Check for updates

Effects of mechanical grinding on the physicochemical properties of silica aerogels

Rutian Li[1,2], Shuisheng Zeng[1,2], Kai Shen[2]*, Guichao Wang[2] and Jun Zhang[1,2]

[1]CCCC Qili Ancient Town (Ganzhou) Cultural Tourism Co., Ltd., Ganzhou, China, [2]School of Resource and Safety Engineering, Central South University, Changsha, China

Mechanical grinding is a facile method to get silica aerogels (SAs) with various particle sizes. However, the relationship between the grinding parameters and physicochemical properties is still unclear. In this study, we concentrated on the effects of grinding time and grinding speed on the physical and chemical properties of silica aerogels. The results reveal that the physicochemical properties of silica aerogels are more sensitive to the grinding speed rather than the grinding time. When the grinding speed is over 200 rpm, large particles of silica aerogels are crushed into smaller particles with obviously decreasing particle sizes and the silica skeletons of silica aerogels have collapsed. The reduction of particle sizes and the collapse of skeleton lead to an increase in both the tap density and thermal conductivity. Therein, the thermal conductivity is positively proportional to the density. Furthermore, the grinded silica aerogels powders still possess the contact angles over 135°, indicating the good hydrophobicity. All these demonstrate that the mechanical grinding has evident effects on the microstructure, density, thermal conductivity and particle sizes, which further impact the performance of silica aerogels during the practical applications. Given the expanding applications of SAs across various industries, the study serves as a valuable reference for optimizing the mechanical post-treatment of SAs, facilitating the achievement of desired particle sizes. Ultimately, this research holds great potential in diversifying the application fields of SAs in their powdered form.

KEYWORDS

silica aerogels, mechanical grinding, physicochemical properties, pore size distribution, thermal insulation

1 Introduction

Silica aerogels (SAs) are typical mesoporous materials (Pierre and Pajonk, 2002), which are synthesized for the first time in 1931 (Kistler, 1931). The common SAs are composed of over 95% pores and less than 5% silica skeletons (Hüsing and Schubert, 1998), which make them possess exceptional properties, such as an ultra-low density, incredibly low thermal conductivity, and a high specific surface area (Pisal and Rao, 2016; Pisal and Venkateswara Rao, 2017). The excellent properties render SAs ideally suited for a wide range of applications, such as thermal insulation (Baetens et al., 2011; Koebel et al., 2012; Cuce et al., 2014), catalyst supports (Pierre, 2010; Zhao et al., 2011), separation (Yu et al., 2015), liquid/gas adsorption (Woermeyer et al., 2012; Mahani et al., 2018; Wu et al., 2018), and aerospace applications (Randall et al., 2011; Bheekhun et al., 2013). As the fast and

cost-effective preparation technology (Koebel et al., 2016; Huber et al., 2017), the application scale and fields will continuously increase in the near future (Smirnova and Gurikov, 2018).

The preparation of SAs commonly comes from the typical sol-gel two-step method (Rao and Bhagat, 2004; Hegde et al., 2007), which can control the size and microstructure of aerogels better (Khedkar et al., 2020). As for the drying technologies, supercritical drying (Rao, 2019) and ambient pressure drying (Khedkar et al., 2019) are usually accepted. However, regardless of SAs are prepared by supercritical drying or ambient pressure drying, the inherent fragility limits the applications of SAs severely (Zhou et al., 2018), which more or less is related to the attribution of silicon-oxygen bond and nanoporous structure. Under this circumstance, different strategies have been carried out to avoid the fragility of SAs, including grafting functional groups to react with other reactive monomers or polymers (Li et al., 2016a), straightforward preparing SA/composites (Joanna et al., 2015; Li et al., 2016a; 2016b) or using SA granules or powder directly (Akimov, 2003). Here we focus on the usage of SA granules or powder due to the great compatibility in current usages, such as aerogel coatings or slurry for the thermal insulation (Kim and Hyun, 2003; Li et al., 2019).

At present, the SA granules or powder are usually used as fillers directly or combined with other substances to meet some requirements in the practical applications (Kanakarajan et al., 2015; Mazrouei-Sebdani et al., 2015; Orth et al., 2017; Sathish Kumar et al., 2017; Maghsoudi and Motahari, 2018; Sedighi et al., 2022). For example, the aerogel-filled insulating brick (aero-brick) (Wernery et al., 2017) and the aerogel incorporated concrete (Gao et al., 2014; Ng et al., 2015; Julio et al., 2016; Schnellenbach-Held et al., 2016; Zeng et al., 2018) both adopt SA granules or powder as the raw materials. Maghsoudi (Maghsoudi and Motahari, 2018) added aerogel particles to epoxy resin to prepare aerogel epoxy composites and explored their mechanical, thermal and hydrophobic properties. In these applications, SAs play a role in thermal insulation without standing any external force, which can be protected and wrapped by the robust external components, such as the cement matrix (Li et al., 2019). Thereinto, the SA granules or powder can be obtained from some specific preparation technologies (He et al., 2015; Pan et al., 2017; Stojanovic et al., 2019) or industrial grade aerogel directly. However, the particle size of the SAs is uneven, which results in a nonuniform mixture. Therefore, the postprocessing on as-prepared SAs is essential to get the desired particle sizes in the practical applications.

In order to customize SAs with specific particle sizes, the common and simple approach is mechanical grinding. Since its three-dimensional nanoporous microstructure and frangibility (Randall et al., 2011; Huang et al., 2020), the effects of grinding process on the performance of SAs are supposed to be quite different from those of other materials. Assume that a high grinding speed crushes the SA larger particles into smaller ones, the nanoporous silica skeleton would be damaged at the same time. Subsequently, the pore size distribution would also be changed, which would further influence the thermal insulation performance of SAs (Lu et al., 1992). That is to say, the physical and chemical properties of SAs are deeply affected by the mechanical grinding. However, the relationship between the grinding parameters and physicochemical properties of SAs are remained unclear. Therefore, the systematic

study is needed to investigate the effects of the mechanical grinding on the physicochemical properties of SAs.

Here, we focus on the effects of mechanical grinding on the physicochemical properties of SAs in this work. Thereinto, the effects of grinding time and speed on the physical and chemical properties of SAs were investigated in detail, such as the particle size distribution, tap density, thermal conductivity, microstructure, and surface chemistry. As we all know, SAs have been well applied in continuously increasing industries, these results would provide references for the mechanical post-treatment of SAs, it is beneficial to broaden the application fields of SAs in the powder state significantly.

Previous studies have predominantly focused on the influence of grinding on particle size reduction, neglecting the broader understanding of grinding effects on the physical and chemical properties of aerogels. In this study, we present a comprehensive investigation into the impact of mechanical grinding on the physicochemical properties of SAs. Specifically, we examine the effects of grinding time and speed on crucial properties including particle size distribution, tap density, thermal conductivity, microstructure, and surface chemistry. Given the expanding applications of SAs across various industries, our findings serve as a valuable reference for optimizing the mechanical post-treatment of SAs, facilitating the achievement of desired particle sizes. Ultimately, this research holds great potential in diversifying the application fields of SAs in their powdered form.

2 Experimental section

## 2.1 Materials and grinding instrument

SAs were purchased from Guangdong Alison Hi-tech Co., Ltd. The vertical planetary ball grinder (XQM-4A, Changsha Tiancheng Powder Technology CO., Ltd., China), polytetrafluoroethylene tanks and agate balls were employed to grind SAs. The grinding instrument and components are presented in Figure 1.

Firstly, SAs were pre-grinded by hands to break larger blocks into small pieces. Then, each 10 g pre-grinded SAs were placed into a polytetrafluoroethylene tank with configured agate balls. Subsequently, the grinder was launched as per the presupposed grinding parameters listed in Table 1. In order to ensure the accuracy of the experiment, each grinding condition was repeated three times. In this study, the effects of grinding time and grinding speed were explored accordingly.

2.2 Characterization

The tap density (ρ) was measured by the tapping apparatus (ZS-202, China) with a measuring cylinder of 25 mL at the vibration frequency of 300 rpm for 10 min. The thermal conductivity was measured via a thermal conductivity meter (TC3000E, XIATECH, China) using a transient hot-wire method at room temperature under ambient pressure. The field emission scanning electron microscope (SEM, SIRION 200, FEI) was used to observe the microstructure of SAs. Moreover, based on the nitrogen adsorption-desorption tests, the specific surface areas were calculated using the
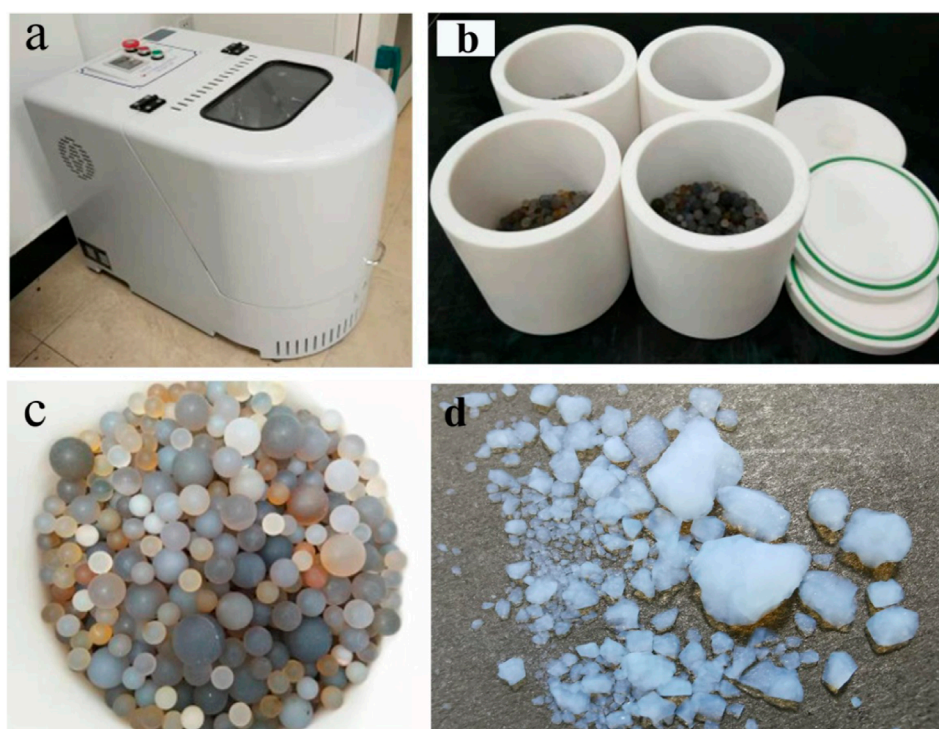
FIGURE 1
(A) Vertical planetary ball grinder, **(B)** polytetrafluoroethylene tanks, **(C)** agate balls, **(D)** silica aerogel.

TABLE 1 Grinding parameters in this study.

Factors	Presupposed values
grinding time (min)	15, 30, 45, 60
grinding speed (rpm)	100, 200, 300

Brunauer–Emmett–Teller (BET) method (Brunauer et al., 1938). The pore parameters were calculated by Barrett–Joyner–Halenda (BJH) method (Barrett et al., 1951), respectively. The functional groups and chemical bonds of SAs were studied by Fourier transform infrared spectroscopy (FTIR) using Nicolet iS50 (Thermo, USA) with the KBr pellet method. The hydrophobicity was tested by the contact angle meter (Shanghai Zhongchen Instrument JC 2000D1, China), in which a 5 uL water droplet was dropped on the sample surface, and the contact angles were obtained by the image processing program, ImageJ (Schneider et al., 2012). The particle size distribution (PSD) of SAs was evaluated by a particle size analyzer (Malvern Mastersizer 3000, England) and the dry test mode was employed.

3 Results and discussion

3.1 Particle size distribution

Figure 2 presents the particle size distribution (PSD) of grinded SAs under different conditions. The PSD curve of the original SAs and those of SAs grinded at 100 rpm are nearly identical, presenting the wide range from 0.1 um to 1000 um with three peaks, which indicates that the grinding speed of 100 rpm has little effect on the PSD of SAs. As the grinding speed increases to 200 rpm or 300 rpm, the PSD approximates the normal distribution, And the peaks of SAs grinded at 300 rpm is much narrower and higher than those grinded at 200 rpm, which indicates that a more uniform PSD can be obtained at a higher grinding speed. Furthermore, it is observed, based on the findings depicted in Figure 2, that the duration of grinding exerts minimal influence on the particle size distribution (PSD). Figure 3 presents a comprehensive overview of the characteristic parameters associated with the particle size, specifically the cumulative distribution percentages corresponding to 50% (D_{50}) and 90% (D_{90}). Interestingly, it is discovered that a higher grinding speed significantly reduces both D_{50} and D_{90} values, while the impact of grinding time on these two parameters appears to be constrained.

In other words, the influence of the grinding speed on the particle size of SAs is more significant than that of the grinding time. During the mechanical grinding process, for a fixed grinding speed, the grinding energy is unchanged despite of increasing grinding time, which is hard to continuously crush particles into much smaller ones. Because the surface free energy of SAs increases with the particle size decreasing (Wang and Wang, 1999), more external energy is needed to refine the SA powder. With the increase of grinding speed, more energy is supplied, which ensures that SAs can be grinded into finer particles easily, leading to a significant reduction in particle size. Therefore, increasing the grinding speed can refine SA powder more effectively rather than prolonging the grinding time.
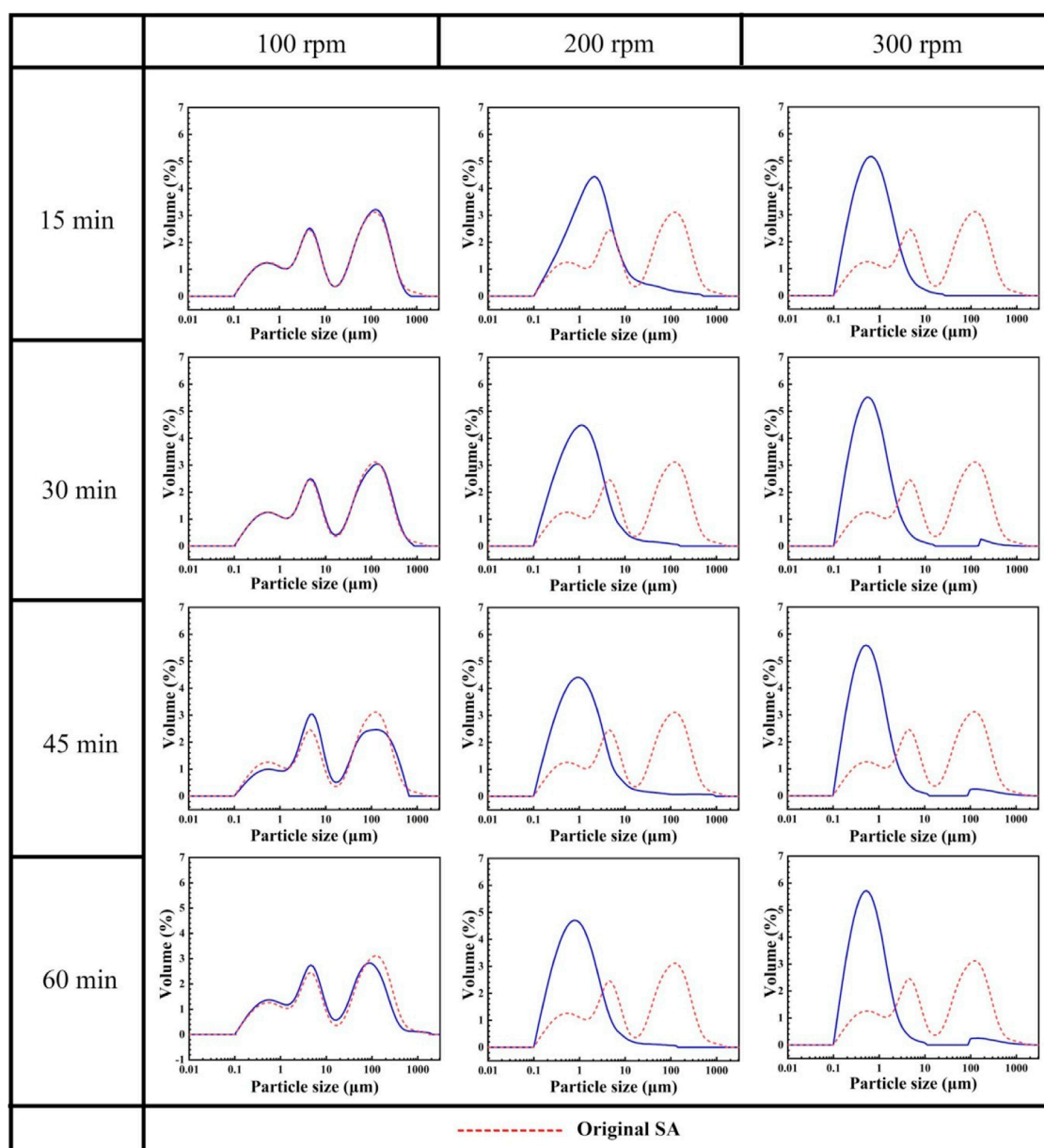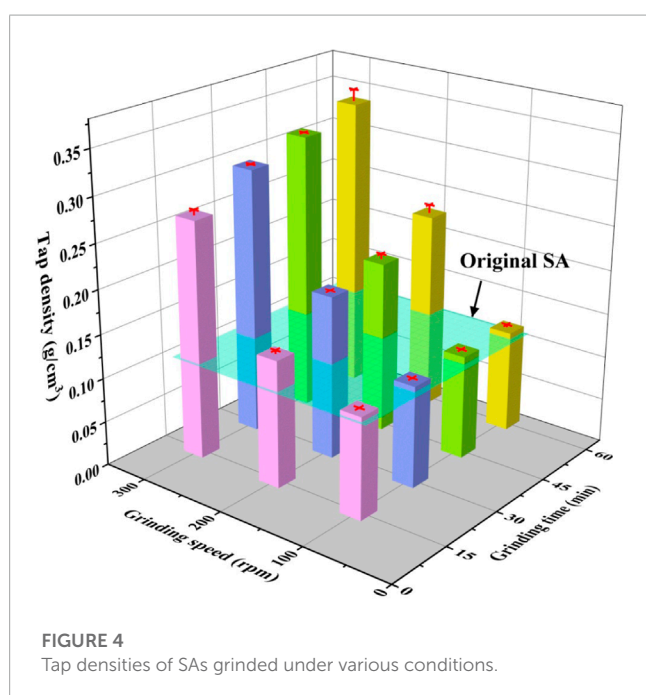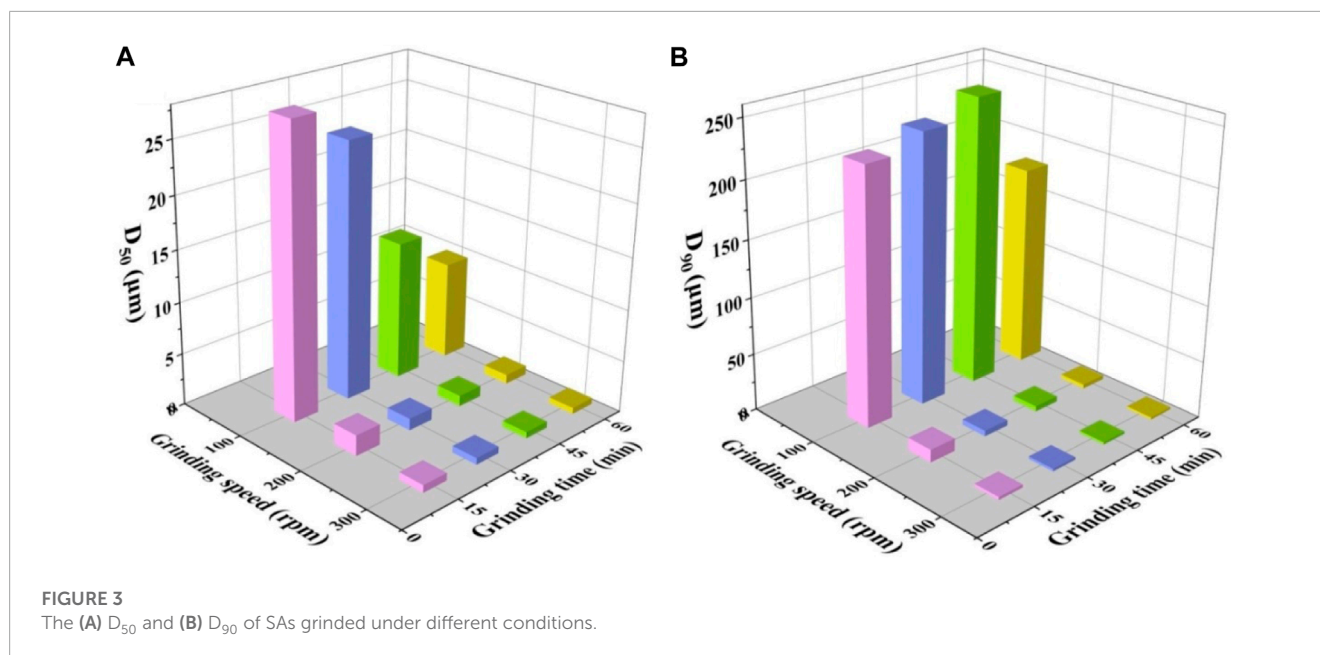
FIGURE 2
The PSD of SAs under different grinding conditions.

3.2 Tap density

The tap densities of SAs grinded under different conditions are presented in Figure 4, in which the tap density of the original SAs is 0.11 g/cm^3. With a fixed grinding time, an escalating grinding speed from 100 rpm to 300 rpm results in an approximate twofold increase in tap density. Conversely, at a constant grinding speed of 300 rpm, a rise in the grinding time from 15 min to 60 min, leads to a mere 22% increase in tap density. Notably, SAs ground at 100 rpm exhibit tap densities that remain comparable to the original SAs, hovering around 0.12 g/cm^3. Conversely, SAs subjected to grinding at 300 rpm manifest tap densities that are on average three times greater than those of the untreated SAs. Hence, for a

specific grinding time, a substantial surge in tap density is observed with increasing grinding speed, while the effect of grinding time on tap density remains relatively modest at a fixed grinding speed. These observations underscore the greater sensitivity of tap density to grinding speed as opposed to grinding time.

As elucidated earlier, it has been established that lower grinding speeds inadequately facilitate the refinement of SA particles due to insufficient energy input. However, a notable surge in grinding energy can be achieved by employing higher grinding speeds, thereby supplying ample energy to effectively refine the SA particles. Building upon the aforementioned analyses and results, the observed increase in tap density under higher grinding speeds is deemed to be closely associated with microstructural variations,

FIGURE 3
The **(A)** D_{50} and **(B)** D_{90} of SAs grinded under different conditions.

FIGURE 4
Tap densities of SAs grinded under various conditions.

which will be thoroughly examined and expounded upon in the subsequent discussion.

3.3 Microstructure

Figure 5 shows the microstructure of SAs under different grinding conditions. Obviously, the grinding process causes the reduction of SA particle size. As the grinding speed increases, the large particles are gradually crushed into smaller particles. Specifically, some large particles are still observed at the grinding

speed of 100 rpm, while these particles are broken into smaller particles when the grinding speed over 200 rpm. Although some smaller particles aggregate again due to the electrostatic interaction, the particle size still decreases as a whole. Under a higher grinding speed, the superimposition of the rotary bias pressure generated higher energy, which destroys the nanoporous silica skeletons of SAs easily. Under these circumstances, the grinding process leads to the generation of SAs featuring smaller-sized particles, accompanied by the gradual elimination of certain pores as a consequence of the collapse of silica skeletons. Consequently, the resultant SA powder exhibits a higher density and diminished pore structure within its particles. As previously highlighted, the tap density exhibits a rapid ascent in tandem with increasing grinding speed. Therefore, it is postulated that the observed augmentation in tap density stems from a combination of particle size reduction and the collapse of silica network skeletons within the SAs.

3.4 Nitrogen sorption

To further verify the effects of mechanical grinding on the microstructure of SAs, the nitrogen adsorption-desorption isotherms of SAs grinded under different conditions were measured. As presented in Figure 6, the adsorption-desorption isotherms in Figures 6A, B all belong to the type IV isotherms and the H3 hysteresis loops are observed (Li et al., 2018), which respectively indicates the attribution of mesoporous materials and the existence of slit-like pores (Rojas et al., 2002; Lermontov et al., 2014). Nevertheless, the relationship between the nitrogen adsorbed quantity and the grinding condition is unclear.

At the grinding time of 30 min in Figure 6C, the most probable pore diameter at the grinding speed of 100 rpm is almost the same as that of the original SAs. With the grinding speed increasing, the most probable pore diameter decreases to about 40 nm and 12 nm at the grinding speed at 200 rpm and 300 rpm, respectively. When
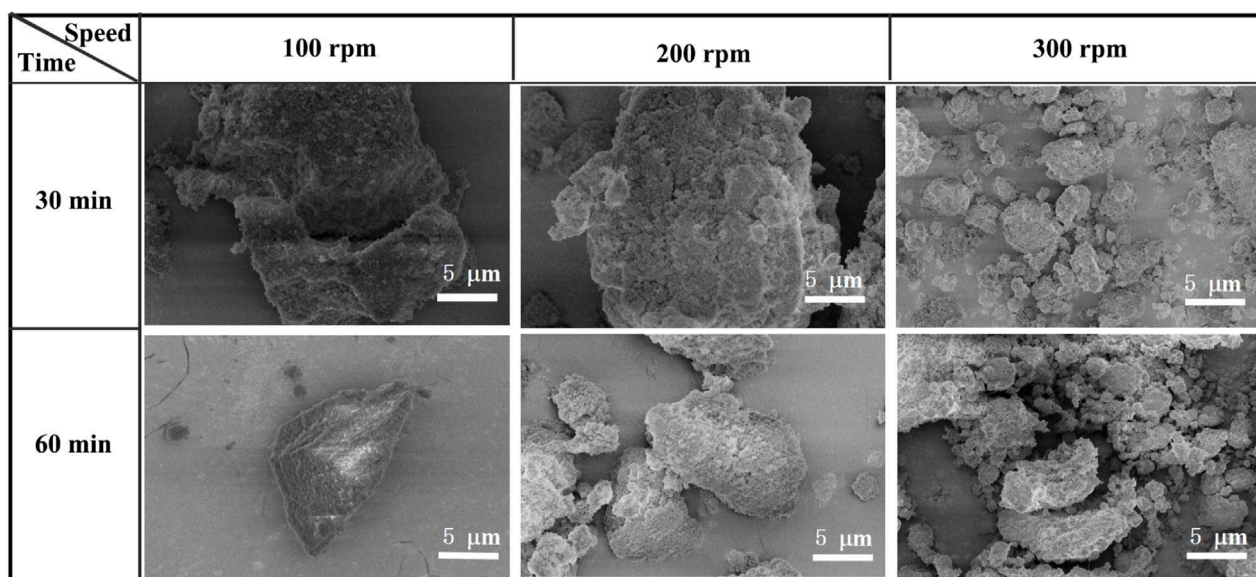
FIGURE 5
The microstructure of SAs grinded under different conditions.

the grinding time increases to 60 min in Figure 6D, the similar most probable pore diameters are observed at the corresponding grinding speed. Considering that SAs are consisted of abundant nanopores (including micropores, mesopores and macropores) and nano-sized silica skeletons (Li et al., 2015), the reduction in pore size is easy to occur with the collapse of the network skeletons during the grinding process. It further indicates that suitable mechanical grinding conditions can adjust the particle size of SAs without changing the attribution of mesoporous materials.

The detailed pore parameters of SAs grinded under various conditions are listed in Table 2. The investigation reveals that the BET surface areas of SAs exhibit a consistent concentration of approximately 300 m^2/g across diverse grinding conditions. However, notable reductions are observed in both pore volume and average pore size. Despite the occurrence of network skeleton collapse during the grinding process, the fundamental characteristic of mesoporous materials in the ground SAs remains intact. Nevertheless, it is inevitable that the pore structure undergoes modifications due to the decrease in pore volume and pore size.

3.5 Chemical property and hydrophobicity

The FTIR spectrums of SAs under different grinding conditions are presented in Figure 7. The prominent peaks observed at 1000–1100 cm^{-1} correspond to the asymmetric stretching vibration of Si-O-Si bonds (Li et al., 2015; 2018). The broad peaks around 3451 cm^{-1} and 1639 cm^{-1} are due to the stretching vibration of OH bonds (Li et al., 2015). Simultaneously, the asymmetric and symmetric stretching vibrations of C-H bonds are observed around 2971 cm^{-1} and 1409 cm^{-1} (Bhagat and Rao, 2006; Li et al., 2015),

and the symmetric deformation vibration of Si-C bonds appear around 845 cm^{-1} (Gurav et al., 2009). In summary, regardless of variations in grinding speed and grinding time, all tested specimens exhibit identical characteristic chemical groups or bonds associated with SAs, without any emergence of new chemical absorption peaks. This finding conclusively demonstrates that mechanical grinding exerts no discernible influence on the surface chemistry of SAs.

As it is known to all, the hydrophobicity of materials depends on surface chemistry and surface roughness mainly (Venkateswara Rao et al., 2003; Mahadik et al., 2011). The surface chemistry of grinded SAs is still kept the same as the original SAs after the mechanical grinding, which provides the similar chemical basis for the hydrophobicity. The contact angles of SAs grinded under different conditions are shown in Figure 8, in which all the contact angles of the grinded SAs exceed 135°, indicating the grinding process has little effect on the hydrophobicity. To be more specific, the contact angles range from 136° to 145°. This variation of contact angle is related to the change of particle size of the grinded SAs. Despite this, the grinded SAs still can satisfy the requirement of the hydrophobicity for some special application fields.

3.6 Thermal conductivity

The thermal conductivities of SAs under different grinding speeds are shown in Figure 9A. For a fixed grinding speed, the thermal conductivity increases mildly with the grinding time increasing. For example, the thermal conductivity of SAs grinded at 100 rpm rises from 23.6 mW/(m·K) to 24.1 mW/(m·K). These values are very close to the thermal conductivity of the original SAs, 24.5 mW/(m·K), indicating that the grinding speed of 100 rpm
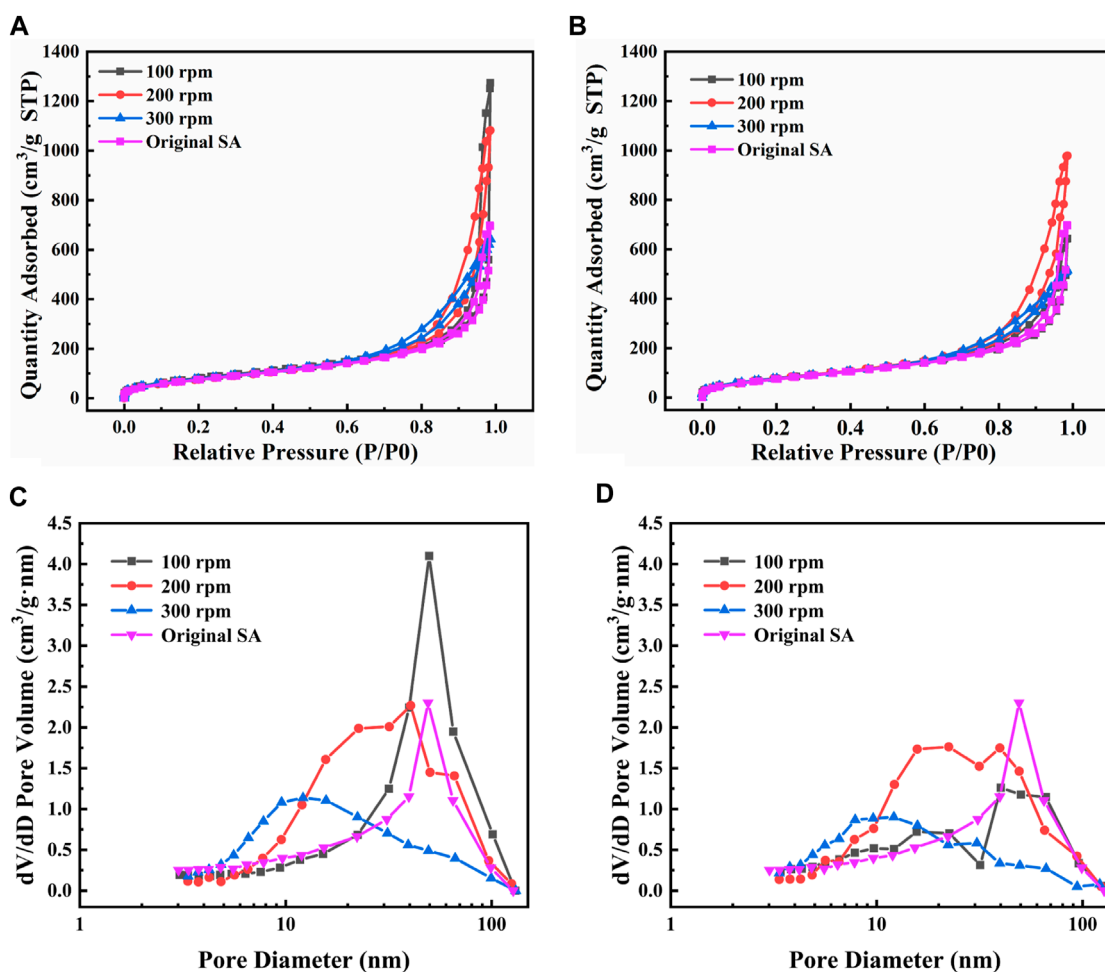
FIGURE 6
Adsorption-desorption isotherms and pore size distribution under different grinding conditions **(A,C)** 30 min and **(B,D)** 60 min.

TABLE 2 Pore parameters of samples under various grinding speeds.

Grinding time (min)	Grinding speed (rpm)	BET surface area (m²/g)	Pore volume (cm³/g)	Average pore size (nm)
0	0	321	1.8	25.4
	100	318	1.9	24.8
30	200	296	1.7	22.6
	300	305	1.0	13.0
	100	300	1.7	21.9
60	200	303	1.5	20.0
	300	298	0.8	10.7

has little impact on the thermal conductivity of SAs. However, the thermal conductivity increases dramatically as the grinding speed increases. At a fixed grinding time of 15 min, the thermal conductivity of SAs grinded under 300 rpm increases 85% compared to that of SAs grinded under 100 rpm. It further finds that the increment of the thermal conductivity caused by the grinding speed also increases with the grinding time.

Figure 9B presents the relationship between the thermal conductivity and the tap density for the grinded SAs, in which the thermal conductivity presents good linearity with the tap
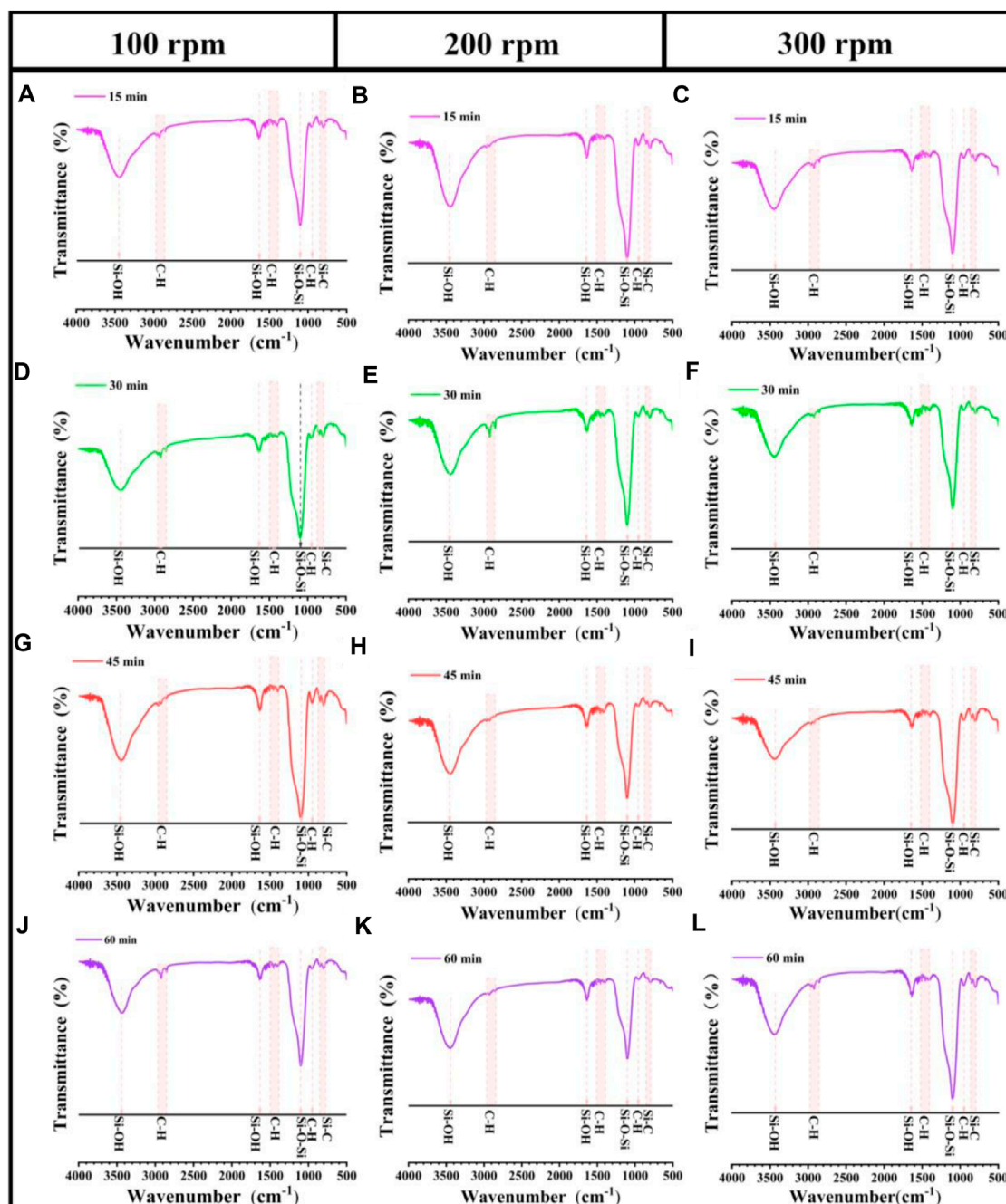
FIGURE 7
FTIR spectra of SAs grinded under different grinding conditions. **(A–C)** 15 min, **(D–F)** 30 min, **(G–I)** 45 min, and **(J–L)** 60 min.

density. Generally, the effective thermal conductivity of SAs can be separated into three parts, i.e., the solid thermal conductivity of silica skeletons, the gaseous thermal conductivity of the air in pores, and the radiative thermal conductivity (Li et al., 2016b). For the ambient temperature, the radiative thermal conductivity is usually neglected. The heat transfer by the air in pores is strictly limited due to the Knudsen effect (Lu et al., 1995), and this effect is more significant with the decreasing pore size. Hence, the gaseous thermal conductivity of SAs is relatively low, usually not exceeding

6 mW/(m·K) under ambient temperature (Li et al., 2016b). The solid thermal conductivity strongly depends on the density, which can be depicted by a power-law relationship between the two (Koebel et al., 2012).

As we discussed previously, the mechanical grinding reduces the particle size of SAs, which simultaneously causes the decrease of pore size and the increase of the tap density. These changes result in the dramatical increase of the solid thermal conductivity, while the gaseous thermal conductivity of SAs just has a small variation in
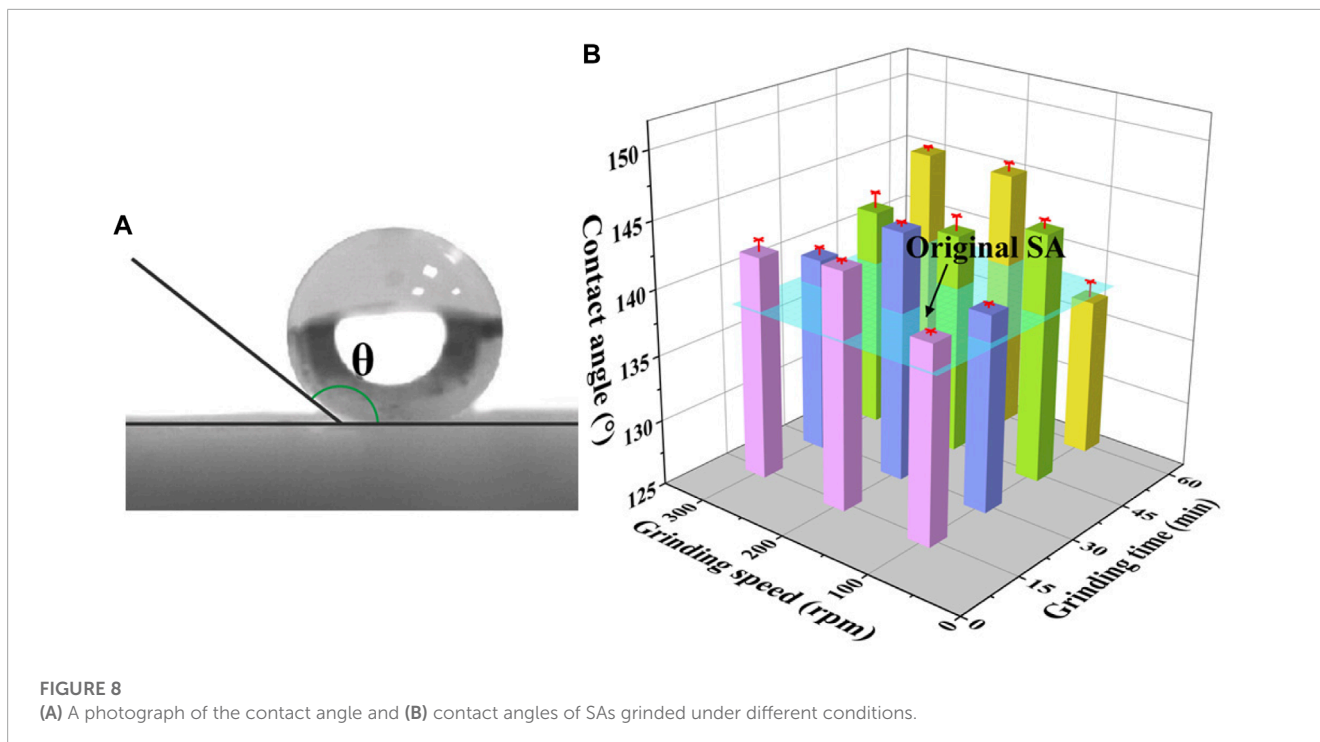
FIGURE 8
(A) A photograph of the contact angle and **(B)** contact angles of SAs grinded under different conditions.
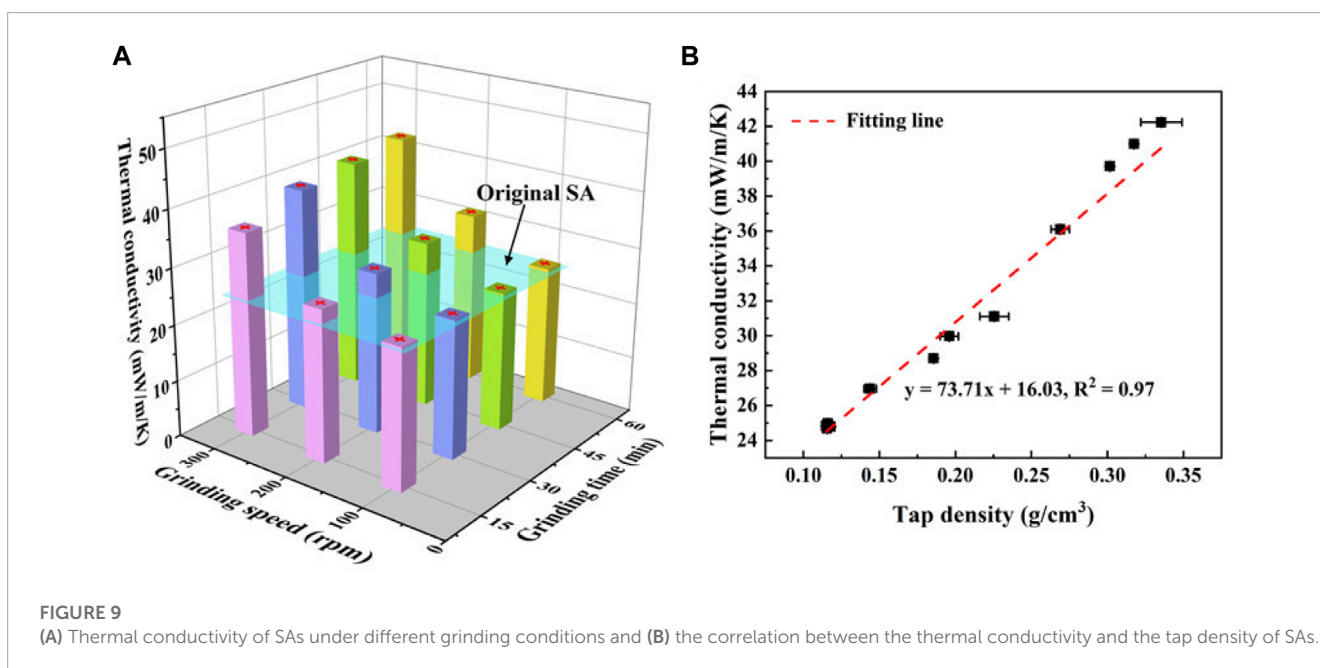

FIGURE 9
(A) Thermal conductivity of SAs under different grinding conditions and **(B)** the correlation between the thermal conductivity and the tap density of SAs.

the range of 2–3 mW/(m·K). As a consequence, the effective thermal conductivity primarily depends on the solid thermal conductivity, which increases significantly with the increasing density.

4 Conclusion

In this study, a comprehensive investigation was conducted to assess the impact of mechanical grinding on the physicochemical

characteristics of SAs. It is determined that adjusting the particle size of SAs through controlled mechanical grinding at speeds exceeding 200 rpm is a viable approach, with the sensitivity of SAs towards grinding speed surpassing that of grinding time. Conversely, lower grinding speeds, not exceeding 100 rpm, exhibit negligible influence on the physicochemical properties of SAs. Microstructural analysis reveals that elevated grinding speeds lead to the disruption of the aerogel network skeleton, resulting in an increase in tap density from 0.09 g/cm^3 to 0.33 g/cm^3.

Simultaneously, it induces a reduction in the pore size distribution, with the average pore size diminishing from 50 nm to 10 nm. It is noteworthy that the chemical properties and hydrophobicity of the aerogels remain unaltered by mechanical grinding. However, escalating grinding speeds and durations lead to the destruction of the aerogel network skeleton, consequently enhancing solid-phase heat conduction. As a result, the thermal conductivity of the aerogels rises from 25 mW/(m·K) to 41 mW/(m·K), detrimentally affecting their thermal insulation properties. These research findings elucidate the influence of mechanical grinding speed and duration on the physicochemical properties of SAs and offer valuable insights for identifying appropriate mechanical grinding parameters to achieve desired particle sizes in SAs.

Data availability statement

The raw data supporting the conclusion of this article will be made available by the authors, without undue reservation.

Author contributions

Writing—original draft, RL and KS; writing—review and editing, KS and GW; visualization, SZ and JZ; investigation, GW and SZ; supervision, RL; and funding acquisition, RL. All authors contributed to the article and approved the submitted version.

Conflict of interest

Authors RL, SZ, and JZ were employed by CCCC Qili Ancient Town (Ganzhou) Cultural Tourism Co., Ltd.

The authors declare that this study received funding from CCCC Qili Ancient Town (Ganzhou) Cultural Tourism Co., Ltd. The funder had the following involvement in the study: RL-Writing the original draft, supervision, and funding acquisition; SZ- visualization and investigation; JZ- visualization.

Publisher's note

All claims expressed in this article are solely those of the authors and do not necessarily represent those of their affiliated organizations, or those of the publisher, the editors and the reviewers. Any product that may be evaluated in this article, or claim that may be made by its manufacturer, is not guaranteed or endorsed by the publisher.

References

Akimov, Y. K. (2003). Fields of application of aerogels (review). *Instrum. Exp. Tech.* 46, 13. doi:10.1023/A:1024401803057

Baetens, R., Jelle, B. P., and Gustavsen, A. (2011). Aerogel insulation for building applications: A state-of-the-art review. *Energy Build.* 43, 761–769. doi:10.1016/j.enbuild.2010.12.012

Barrett, E. P., Joyner, L. G., and Halenda, P. P. (1951). The determination of pore volume and area distributions in porous substances. I. Computations from nitrogen isotherms. *J. Am. Chem. Soc.* 73, 373–380. doi:10.1021/ja01145a126

Bhagat, S. D., and Rao, A. V. (2006). Surface chemical modification of TEOS based silica aerogels synthesized by two step (acid–base) sol–gel process. *Appl. Surf. Sci.* 252, 4289–4297. doi:10.1016/j.apsusc.2005.07.006

Bheekhun, N., Abu, T., Abd, R., and Hassan, M. R. (2013). Aerogels in aerospace: An overview. *Adv. Mater. Sci. Eng.* 2013, 1–18. doi:10.1155/2013/406065

Brunauer, S., Emmett, P. H., and Teller, E. (1938). Adsorption of gases in multimolecular layers. *J. Am. Chem. Soc.* 60, 309–319. doi:10.1021/ja01269a023

Cuce, E., Cuce, P. M., Wood, C. J., and Riffat, S. B. (2014). Toward aerogel based thermal superinsulation in buildings: A comprehensive review. *Renew. Sustain. Energy Rev.* 34, 273–299. doi:10.1016/j.rser.2014.03.017

Gao, T., Jelle, B. P., Gustavsen, A., and Jacobsen, S. (2014). Aerogel-incorporated concrete: An experimental study. *Constr. Build. Mater.* 52, 130–136. doi:10.1016/j.conbuildmat.2013.10.100

Gurav, J. L., Rao, A. V., Rao, A. P., Nadargi, D. Y., and Bhagat, S. D. (2009). Physical properties of sodium silicate based silica aerogels prepared by single step sol-gel process dried at ambient pressure. *J. ALLOYS Compd.* 476, 397–402. doi:10.1016/j.jallcom.2008.09.029

He, S., Li, Z., Shi, X., Yang, H., Gong, L., and Cheng, X. (2015). Rapid synthesis of sodium silicate based hydrophobic silica aerogel granules with large surface area. *Adv. POWDER Technol.* 26, 537–541. doi:10.1016/j.apt.2015.01.002

Hegde, N. D., Hirashima, H., and Rao, A. V. (2007). Two step sol-gel processing of TEOS based hydrophobic silica aerogels using trimethylethoxysilane as a co-precursor. *J. POROUS Mater* 14, 165–171. doi:10.1007/s10934-006-9021-2

Huang, S., Wu, X., Li, Z., Shi, L., Zhang, Y., and Liu, Q. (2020). Rapid synthesis and characterization of monolithic ambient pressure dried MTMS aerogels in pure water. *J. Porous Mater.* 27, 1241–1251. doi:10.1007/s10934-020-00902-3

Huber, L., Zhao, S., Malfait, W. J., Vares, S., and Koebel, M. M. (2017). Fast and minimal-solvent production of superinsulating silica aerogel granulate. *Angew. Chem.-Int. Ed.* 56, 4753–4756. doi:10.1002/anie.201700836

Hüsing, N., and Schubert, U. (1998). Aerogels—airy materials: Chemistry, structure, and properties. *Angew. Chem. Int. Ed.* 37, 22–45. doi:10.1002/(SICI)1521-3773(19980202)37:1/2<22::AID-ANIE22>3.0.CO;2-I

Joanna, C. H. W., Hicret, K., Philippe, T., Samuel, B., and Matthias, M. K. (2015). Mechanical and thermal properties of nanofibrillated cellulose reinforced silica aerogel composites. *Microporous Mesoporous Mater* 217, 150–158. doi:10.1016/j.micromeso.2015.06.025

Julio, M. de F., Soares, A., Ilharco, L. M., Flores-Colen, I., and de Brito, J. (2016). Silica-based aerogels as aggregates for cement-based thermal renders. *Cem. Concr. Compos.* 72, 309–318. doi:10.1016/j.cemconcomp.2016.06.013

Kanakarajan, P., Sundaram, S., Kumaravel, A., Rajasekar, R., and Kumar, P. S. (2015). Acoustic emission testing of surface roughness and wear caused by grinding of ceramic materials. *Mater. Test.* 57, 337–342. doi:10.3139/120.110714

Khedkar, M. V., Jadhav, S. A., Somvanshi, S. B., Kharat, P. B., and Jadhav, K. M. (2020). Physicochemical properties of ambient pressure dried surface modified silica aerogels: Effect of pH variation. *SN Appl. Sci.* 2, 696. doi:10.1007/s42452-020-2463-3

Khedkar, M. V., Somvanshi, S. B., Humbe, A. V., and Jadhav, K. M. (2019). Surface modified sodium silicate based superhydrophobic silica aerogels prepared via ambient pressure drying process. *J. Non-Cryst. Solids* 511, 140–146. doi:10.1016/j.jnoncrysol.2019.02.004

Kim, G. S., and Hyun, S. H. (2003). Synthesis of window glazing coated with silica aerogel films via ambient drying. *J. Non-Cryst. Solids* 320, 125–132. doi:10.1016/s0022-3093(03)00027-9

Kistler, S. S. (1931). Coherent expanded-aerogels. *J. Phys. Chem.* 36, 52–64. doi:10.1021/j150331a003

Koebel, M. M., Huber, L., Zhao, S., and Malfait, W. J. (2016). Breakthroughs in cost-effective, scalable production of superinsulating, ambient-dried silica aerogel and silica-biopolymer hybrid aerogels: From laboratory to pilot scale. *J. SOL-GEL Sci. Technol.* 79, 308–318. doi:10.1007/s10971-016-4012-5

Koebel, M., Rigacci, A., and Achard, P. (2012). Aerogel-based thermal superinsulation: An overview. *J. Sol-Gel Sci. Technol.* 63, 315–339. doi:10.1007/s10971-012-2792-9

Lermontov, S. A., Malkova, A. N., Yurkova, L. L., Straumal, E. A., Gubanova, N. N., Baranchikov, A. Ye., et al. (2014). Diethyl and methyl-tert-buthyl ethers as new solvents for aerogels preparation. *Mater. Lett.* 116, 116–119. doi:10.1016/j.matlet.2013.10.080

Li, P., Wu, H., Liu, Y., Yang, J., Fang, Z., and Lin, B. (2019). Preparation and optimization of ultra-light and thermal insulative aerogel foam concrete. *Constr. Build. Mater.* 205, 529–542. doi:10.1016/j.conbuildmat.2019.01.212

Li, Z., Cheng, X., Gong, L., Liu, Q., and Li, S. (2018). Enhanced flame retardancy of hydrophobic silica aerogels by using sodium silicate as precursor and phosphoric acid as catalyst. *J. Non-Cryst. Solids* 481, 267–275. doi:10.1016/j.jnoncrysol.2017.10.053

Li, Z., Cheng, X., He, S., Shi, X., Gong, L., and Zhang, H. (2016a). Aramid fibers reinforced silica aerogel composites with low thermal conductivity and improved mechanical performance. *Compos. Part Appl. Sci. Manuf.* 84, 316–325. doi:10.1016/j.compositesa.2016.02.014

Li, Z., Cheng, X., He, S., Shi, X., and Yang, H. (2015). Characteristics of ambient-pressure-dried aerogels synthesized via different surface modification methods. *J. Sol-Gel Sci. Technol.* 76, 138–149. doi:10.1007/s10971-015-3760-y

Li, Z., Gong, L., Cheng, X., He, S., Li, C., and Zhang, H. (2016b). Flexible silica aerogel composites strengthened with aramid fibers and their thermal behavior. *Mater. Des.* 99, 349–355. doi:10.1016/j.matdes.2016.03.063

Lu, X., Caps, R., Fricke, J., Alviso, C., and Pekala, R. (1995). Correlation between structure and thermal conductivity of organic aerogels. *J. Non-Cryst. Solids* 188, 226–234. doi:10.1016/0022-3093(95)00191-3

Lu, X., Wang, P., Arduini-Schuster, M. C., Kuhn, J., Büttner, D., Nilsson, O., et al. (1992). Thermal transport in organic and opacified silica monolithic aerogels. *J. Non-Cryst. Solids* 145, 207–210. doi:10.1016/S0022-3093(05)80457-0

Maghsoudi, K., and Motahari, S. (2018). Mechanical, thermal, and hydrophobic properties of silica aerogel–epoxy composites. *J. Appl. Polym. Sci.* 135, 45706. doi:10.1002/app.45706

Mahadik, D., Rao, A., Parale, V., Kavale, M., Wagh, P., Ingale, S., et al. (2011). Effect of surface composition and roughness on the apparent surface free energy of silica aerogel materials. *Appl. Phys. Lett.* 99, 104. doi:10.1063/1.3635398

Mahani, A. A., Motahari, S., and Mohebbi, A. (2018). Sol-gel derived flexible silica aerogel as selective adsorbent for water decontamination from crude oil. *Mar. Pollut. Bull.* 129, 438–447. doi:10.1016/j.marpolbul.2017.10.012

Mazrouei-Sebdani, Z., Khoddami, A., Hadadzadeh, H., and Zarrebini, M. (2015). Synthesis and performance evaluation of the aerogel-filled PET nanofiber assemblies prepared by electro-spinning. *RSC Adv.* 5, 12830–12842. doi:10.1039/c4ra15297b

Ng, S., Jelle, B. P., Sandberg, L. I. C., Gao, T., and Wallevik, O. H. (2015). Experimental investigations of aerogel-incorporated ultra-high performance concrete. *Constr. Build. Mater.* 77, 307–316. doi:10.1016/j.conbuildmat.2014.12.064

Orth, A., Steinbach, S., Dennstedt, A., and Ratke, L. (2017). Aerogel-filled metals: A syntactic cellular material. *Mater. Sci. Technol.* 33, 299–306. doi:10.1080/02670836.2016.1195971

Pan, Y., He, S., Cheng, X., Li, Z., Li, C., Huang, Y., et al. (2017). A fast synthesis of silica aerogel powders-based on water glass via ambient drying. *J. SOL-GEL Sci. Technol.* 82, 594–601. doi:10.1007/s10971-017-4312-4

Pierre, A. (2010). Aerogel catalysts. *Adv. Sci. Technol.* 65, 174–183. doi:10.4028/www.scientific.net/AST.65.174

Pierre, A., and Pajonk, G. (2002). Chemistry of aerogels and their applications. *Chem. Rev.* 102, 4243–4266. doi:10.1021/cr0101306

Pisal, A. A., and Rao, A. V. (2016). Comparative studies on the physical properties of TEOS, TMOS and Na2SiO3 based silica aerogels by ambient pressure drying method. *J. Porous Mater.* 23, 1547–1556. doi:10.1007/s10934-016-0215-y

Pisal, A. A., and Venkateswara Rao, A. (2017). Development of hydrophobic and optically transparent monolithic silica aerogels for window panel applications. *J. Porous Mater* 24, 685–695. doi:10.1007/s10934-016-0305-x

Randall, J. P., Meador, M. A. B., and Jana, S. C. (2011). Tailoring mechanical properties of aerogels for aerospace applications. *ACS Appl. Mater. Interfaces* 3, 613–626. doi:10.1021/am200007n

Rao, A., and Bhagat, S. (2004). Synthesis and physical properties of TEOS-based silica aerogels prepared by two step (acid-base) sol-gel process. *SOLID STATE Sci.* 6, 945–952. doi:10.1016/j.solidstatesciences.2004.04.010

Rao, A. V. (2019). Elastic superhydrophobic and water glass-based silica aerogels and applications. *J. Sol-Gel Sci. Technol.* 90, 28–54. doi:10.1007/s10971-018-4825-5

Rojas, F., Kornhauser, I., Felipe, C., Esparza, J. M., Cordero, S., Domínguez, A., et al. (2002). Capillary condensation in heterogeneous mesoporous networks consisting of variable connectivity and pore-size correlation. *Phys. Chem. Chem. Phys.* 4, 2346–2355. doi:10.1039/b108785a

Sathish Kumar, P., Pal, S. K., Chinnasamy, M., and Rajasekar, R. (2017). "Organic/silica nanocomposite membranes," in *Organic-inorganic composite polymer electrolyte membranes: Preparation, properties, and fuel cell applications*. Editors D. Inamuddin, A. Mohammad, and A. M. Asiri (Cham, Germany: Springer), 47–72. doi:10.1007/978-3-319-52739-0_3

Schneider, C. A., Rasband, W. S., and Eliceiri, K. W. (2012). NIH image to ImageJ: 25 years of image analysis. *Nat. Methods* 9, 671–675. doi:10.1038/nmeth.2089

Schnellenbach-Held, M., Welsch, T., Fickler, S., Milow, B., and Ratke, L. (2016). Development of high performance aerogel concrete. *Bet. STAHLBETONBAU* 111, 555–563. doi:10.1002/best.201600017

Sedighi, S., Khoddami, A., Izadan, H., Alsharif, M. A., and Naeimirad, M. (2022). The influence of silica aerogels on physical, mechanical, and morphological properties of melt-spun POY and DTY polyester yarns. *Polym. Test.* 112, 107628. doi:10.1016/j.polymertesting.2022.107628

Smirnova, I., and Gurikov, P. (2018). Aerogel production: Current status, research directions, and future opportunities. *J. Supercrit. FLUIDS* 134, 228–233. doi:10.1016/j.supflu.2017.12.037

Stojanovic, A., Zhao, S., Angelica, E., Malfait, W. J., and Koebel, M. M. (2019). Three routes to superinsulating silica aerogel powder. *J. SOL-GEL Sci. Technol.* 90, 57–66. doi:10.1007/s10971-018-4879-4

Venkateswara Rao, A., Kulkarni, M. M., Amalnerkar, D. P., and Seth, T. (2003). Superhydrophobic silica aerogels based on methyltrimethoxysilane precursor. *J. Non-Cryst. Solids* 330, 187–195. doi:10.1016/j.jnoncrysol.2003.08.048

Wang, J., and Wang, X. (1999). The change of behavior of powder during the course of ball milling. *J. Gansu Univ. Technol.*

Wernery, J., Ben-Ishai, A., Binder, B., and Brunner, S. (2017). Aerobrick - an aerogel-filled insulating brick. *Sustain. ENERGY Build.* 134, 490–498. doi:10.1016/j.egypro.2017.09.607

Woermeyer, K., Alnaief, M., and Smirnova, I. (2012). Amino functionalised Silica-Aerogels for CO2-adsorption at low partial pressure. *Adsorpt.-J. Int. Adsorpt. Soc.* 18, 163–171. doi:10.1007/s10450-012-9390-6

Wu, Z., Zhang, L., Li, J., Zhao, X., and Yang, C. (2018). Organic-inorganic hybridization for the synthesis of robust *in situ* hydrophobic polypropylsilsesquioxane aerogels with fast oil absorption properties. *RSC Adv.* 8, 5695–5701. doi:10.1039/c7ra13165h

Yu, Y., Wu, X., and Fang, J. (2015). Superhydrophobic and superoleophilic "sponge-like" aerogels for oil/water separation. *J. Mater. Sci.* 50, 5115–5124. doi:10.1007/s10853-015-9034-9

Zeng, Q., Mao, T., Li, H., and Peng, Y. (2018). Thermally insulating lightweight cement-based composites incorporating glass beads and nano-silica aerogels for sustainably energy-saving buildings. *ENERGY Build.* 174, 97–110. doi:10.1016/j.enbuild.2018.06.031

Zhao, Y., Liang, Y., Zhao, X., Jia, Q., and Li, H. (2011). Preparation and microstructure of CuO-CoO-MnO/SiO2 nanocomposite aerogels and xerogels as catalyst carriers. *Prog. Nat. Sci. Mater. Int.* 21, 330–335. doi:10.1016/S1002-0071(12)60065-3

Zhou, T., Cheng, X., Pan, Y., Li, C., Gong, L., and Zhang, H. (2018). Mechanical performance and thermal stability of glass fiber reinforced silica aerogel composites based on co-precursor method by freeze drying. *Appl. Surf. Sci.* 437, 321–328. doi:10.1016/j.apsusc.2017.12.146